Monthly Notices
of the
ROYAL ASTRONOMICAL SOCIETY

MNRAS **513,** 4045–4056 (2022)
Advance Access publication 2022 April 25

https://doi.org/10.1093/mnras/stac1101

# Constraining equation-of-state groups from *g*-mode asteroseismology

Hao-Jui Kuan [1,2★] Christian J. Krüger,[1] Arthur G. Suvorov[1,3] and Kostas D. Kokkotas[1]

[1]*Theoretical Astrophysics, IAAT, University of Tübingen, D-72076 Tübingen, Germany*
[2]*Department of Physics, National Tsing Hua University, Hsinchu 300, Taiwan*
[3]*Manly Astrophysics, 15/41-42 East Esplanade, Manly, NSW 2095, Australia*

Accepted 2022 April 13. Received 2022 April 13; in original form 2022 January 11

## ABSTRACT

Buoyancy-restored modes inside neutron stars depend sensitively on both the microphysical (e.g. composition and entropy gradients) and macrophysical (e.g. stellar mass and radius) properties of the star. Asteroseismology efforts for *g* modes are therefore particularly promising avenues for recovering information concerning the nuclear equation of state. In this work, it is shown that the overall low-temperature *g*-space consists of multiple groups corresponding to different classes of equation of state (e.g. hadronic versus hybrid). This is in contrast to the case of pressure-driven modes, for example, which tend to follow a universal relation regardless of microphysical considerations. Using a wide library of currently viable equations of state, perturbations of static, stratified stars are calculated in general relativity to demonstrate in particular how *g*-space groupings can be classified according to the mean mass density, temperature, central speed of sound, and tidal deformability. Considering present and future observations regarding gravitational waves, accretion outbursts, quasi-periodic oscillations, and precursor flashes from gamma-ray bursts, it is shown how one might determine which group the *g* modes belong to.

**Key words:** asteroseismology – gravitational waves – radiation mechanisms: non-thermal – stars: neutron – stars: oscillations (including pulsations) – equation of state.

## 1 INTRODUCTION

Neutron stars (NSs), with their extremely high core densities, reside in an otherwise hard-to-realize region of the quantum chromodynamics (QCD) phase diagram. The details of the (supra-)nuclear equation of state (EOS) can only be accessed by connecting their observed outbursts or manifestations with, for example, theoretical predictions of the quasi-normal mode (QNM) spectrum, the maximal supportable mass, and gravitational radiation. Although substantial progress regarding constraints on the EOS from, e.g. the tidal deformability measured by the phase shift in the gravitational waveform for merging binaries (Abbott et al. 2018; De et al. 2018; Raithel, Özel & Psaltis 2018) and observations of the moments of inertia (Greif et al. 2020) have been made in the literature, uncertainties remain and a wide pool of possibilities remain viable. Universal relations between certain stellar properties, however, offer additional avenues that are EOS independent to infer inaccessible unknowns, and thus can indirectly narrow the space of valid candidate descriptions for the stellar interior.

In particular, the QNM spectrum of a NS is strongly associated with the global properties of the star, in the sense that several universal expressions relating mode frequencies and/or damping times to the bulk quantities of the star, like average density, moment of inertia, and tidal Love number, have been established for the *f*, *p*, and *w* modes (Andersson & Kokkotas 1998; Lau, Leung & Lin 2010; Chan et al. 2014; Krüger & Kokkotas 2020; Benitez et al. 2021; Sotani & Kumar 2021). This EOS-insensitive information provides hope for independent constraints by offering a critical tool in rephrasing the detected quantities in terms of others. For example, the mutual tidal deformability of a not-too-massive NSNS binary equates, in a roughly one-to-one fashion, into a compactness of the long-lived remnant because the *f*-mode properties of both the pre-merging and post-merger stars follow the same universal relation (Manoharan, Krüger & Kokkotas 2021). To account for the compositional structure, universal relations for *g* modes, which distinguish one chemical configuration from another, need to be established.

In this article, we aim to introduce some global formulae for *g* modes of NSs in various configurations and at various stages of their lives, either isolated or in binaries. The frequencies of this class of oscillatory modes are encoded in the Brunt–Väisälä frequency, which measures the mismatch in the adiabatic index between the equilibrium and the mode-driven motions (see e.g. Lai 1994). Using the (non-isentropic) general-relativistic pulsation equations, one of our main results is that we can encapsulate the Brunt–Väisälä frequency into *the temperature-modified mean density* of the star, and draw a relation to the *g*-mode frequency, viz.

$$f_{\rm g} \propto \rho_{\rm mean}^{(1-\varsigma)/2} T, \tag{1}$$

for some EOS- and mode-number-dependent constant $-0.7 \lesssim \varsigma \lesssim 0.5$ (see Section 2). We also obtain two invertible mappings for the *g*-mode frequencies in terms of the *central speed of sound*, $v_{\rm s}$, and *tidal deformability*, $\Lambda$, expressed as

$$\log\left(\frac{f_{\rm g_1}}{100\ {\rm Hz}} M\right) = \sum_{i=0}^{3} a_i (\log\Lambda)^i, \tag{2}$$

$$\frac{f_{\rm g_1}}{100\ {\rm Hz}}\left(\frac{v_{\rm s}}{R}\right) = \sum_{i=0}^{3} b_i (\rho_{\rm mean})^{i/2}, \tag{3}$$

★ E-mail: hao-jui.kuan@uni-tuebingen.de

with certain coefficients $\{a_i\}$ and $\{b_i\}$, stellar mass $M$, and radius $R$. Importantly, the first relation (1) divides EOS into three quotient sets, and introduces the concept of *g-space*, which characterizes a specific EOS in terms of the $g$-mode spectrum. This occurs essentially because $\varsigma$ takes values in different blocks for different EOS families in a sense that is made precise in the main text. By representing a (hypothetically) observed $g$ mode as a point in $g$-space, we can, in principle, place constraints on the associated EOS for a wide range of systems, including pulsars, progenitors of binary mergers, and the remnants of mergers. On the other hand, the latter two relations (2) and (3) are common for the set of 20 EOSs considered in this article (i.e. the $a_i$ and $b_i$ are roughly constant among EOSs). Leveraging this universality, we can deduce certain otherwise inaccessible quantities from $g$-mode observables.

Although still a matter of debate, it has been suggested that various NS phenomena may be triggered by the excitation of $g$ modes. For instance, a small percentage of short gamma-ray bursts display precursor phenomena (Coppin, de Vries & van Eijndhoven 2020; Wang et al. 2020), where energetic flashes are observed even many seconds prior to the main event in some cases. If the stellar oscillation modes briefly come into resonance with the orbital motion while the stars are inspiralling, significant amounts of tidal energy may be deposited into the mode(s), possibly to the point that the crust yields due to the exerted shear stresses exceeding the elastic maximum (Tsang et al. 2012; Tsang 2013). $g$ modes in particular appear to lie in a sweet spot, frequency wise, where the expected mode frequencies match the orbital frequency at the time of the precursor flashes (Kuan, Suvorov & Kokkotas 2021a,b). Similarly, $g$-mode frequencies match those observed in quasi-periodic oscillations (QPOs) of X-ray light curve from several NS systems and thus provide another promising avenue for detecting $g$ modes (see e.g. Strohmayer & Mahmoodifar 2014, for such speculation).

In addition, a new and quite important asteroseismological relation emerged through this study connecting the $f$-mode frequency $f_{\rm f}$, with the radius and tidal deformability of an oscillating NS

$$\log\left(\frac{f_{\rm f}}{\rm kHz}R\right)=\sum_{i=0}^{2}c_i(\log\Lambda)^i\,. \tag{4}$$

This relation can be considered as complementary to the one by Chan et al. (2014).

This paper is organized as follows: We introduce the grouping of EOS in terms of the range of $g$-mode frequencies, and we discuss the tidal effects of $g$ modes in Section 2. We then turn to investigate the uniformity among the EOS set considered, producing some universal relations of $g$ modes in Section 3. We speculate some circumstances, where we may be able to detect $g$-mode frequencies in Section 4. A discussion on the possible application of the obtained results is offered in Section 5. Some EOSs are found to allow for NSs with $g$ modes immune to external tidal field, which is discussed in Appendix A.

Except where stated otherwise, we adopt the normalization of $10\ {\rm km}=1=1\ {\rm M}_\odot$ for the radius and mass of stars, and we reduce the dimension of velocity by unitizing the speed of light, $c=1$.

## 2 *G*-MODE GROUPING

We consider non-rotating, spherically symmetric equilibrium stellar models, obtained as solutions to the Tolman–Oppenheimer–Volkoff equations (Oppenheimer & Volkoff 1939; Tolman 1939), for several EOSs approximated by piece-wise polytropic segments (Read et al. 2009; O'Boyle et al. 2020); see Table 1 for the EOS list, and Fig. 1 for their mass-to-radius relations. The EOSs are chosen to cover a wide range, from those obtained for NSs with purely *nepμ* matters, to those influenced by the hypothetically existing hyperons (e.g. GNH3, H4) possibly even displaying phase transition to free quarks (i.e. hybrid stars; e.g. ALF2). Although some of the considered EOSs cannot support the heaviest pulsar observed to date, namely PSR J0740+6620 (Cromartie et al. 2019) with the mass of $\sim$2.14 $\rm M_\odot$, they are included for the sake of demonstrating the generality of the trifurcation of EOS space, while we note that only EOSs in Group I support the mass of PSR J0740+6620.

The polytropic (adiabatic) index of the star expresses the pressure exerted by a bulk of certain density, and depends on the detailed thermodynamic balance, chemical composition, and degeneracy status of the system (Haensel, Levenfish & Yakovlev 2002). However, weak interactions (e.g. Urca processes) and/or diffusive processes within the star modulate the relative particle abundances over time (Hoyos, Reisenegger & Valdivia 2008; Hoyos, Reisenegger & Valdivia 2010), leading to entropy (McDermott, van Horn & Scholl 1983; Reisenegger & Goldreich 1992) and/or compositional gradients (Finn 1987). These variations permit mobile fluid elements to experience buoyancy whenever perturbed away equilibrium, giving rise to the existence of $g$ modes. The frequencies of these modes therefore

**Table 1.** Fitting index $\varsigma$ defined in equation (6) for a variety of EOSs. Although there are a few outliers, we see that those listed in the first column have $\varsigma\gtrsim 0.2$, the second column features the range 0–0.2, and in the final column are $\varsigma\lesssim 0$.

| Group I | | Group II | | Group III | |
|---|---|---|---|---|---|
| EOS | $\varsigma$ | EOS | $\varsigma$ | EOS | $\varsigma$ |
| APR4[a] | 0.413 | SLy[f] | 0.158 | H4[j] | −0.094 |
| MPA1[b] | 0.321 | WFF3[d] | 0.027 | H7[j] | −0.221 |
| MS1[c] | 0.266 | FPS[g] | 0.011 | GNH3[k] | −0.081 |
| MS1b[c] | 0.333 | BBB2[h] | 0.101 | PAL6[l] | 0.059 |
| WFF1[d] | 0.453 | APR1[a] | 0.128 | PCL2[m] | −0.309 |
| WFF2[d] | 0.461 | BHF[h] | 0.143 | ALF2[n] | −0.657 |
| ENG[e] | 0.179 | KDE0V[i] | 0.200 | – | – |

*Notes.* [a] Akmal, Pandharipande & Ravenhall (1998). [b] Müther, Prakash & Ainsworth (1987). [c] Mueller & Serot (1996). [d] Wiringa, Fiks & Fabrocini (1988). [e] Engvik et al. (1994). [f] Douchin & Haensel (2001). [g] Friedman & Pandharipande (1981). [h] Baldo, Bombaci & Burgio (1997). [i] Agrawal, Shlomo & Au (2005). [j] Lackey, Nayyar & Owen (2006). [k] Glendenning (1985). [l] Prakash, Ainsworth & Lattimer (1988). [m] Prakash, Cooke & Lattimer (1995). [n] Alford et al. (2005).

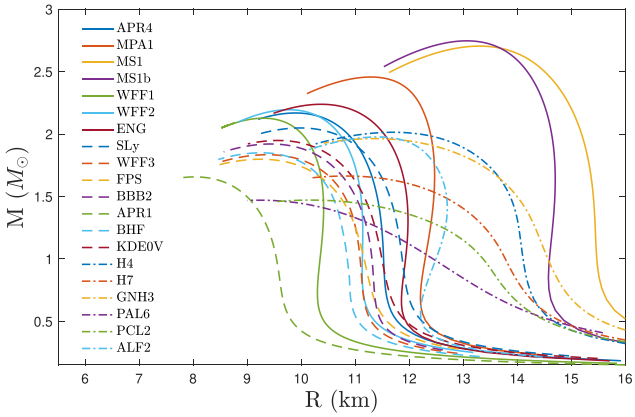


**Figure 1.** Mass–radius diagrams for the EOS considered here (see plot legends).

depend strongly on the strength of the stratification. Assuming that the adiabatic indices for the perturbation ($\Gamma$) and the equilibrium ($\gamma$) have a constant ratio $1 + \delta$, we introduce a simple parametrization for the forces supporting $g$ modes; see Kuan et al. (2021a) for a discussion on the validity of this approximation. We identify $\delta$ with the temperature $T$ of isothermal stars in Section 2.1. Although we find that the correlation between $\delta$ and $T$ holds only for $T \lesssim 10^{10}$ K, we show the validity of the justification for binaries undergoing the tidal heating of $g$ modes in Section 2.2. With respect to the simple parametrization of stratification, three divisions of EOSs are illustrated in Section 2.3. Overtones are denoted by $g_n$ mode, for which the radial eigenfunction has $n$ nodes.

### 2.1 Temperature dependence

We consider EOS to be barotropic at the background level in the present article, hence $g$ modes are supported by the entropy gradient. In general, the temperature profile of NSs in different systems can differ significantly. For instance, mature, isolated NSs are expected to be almost isothermal (Krüger, Ho & Andersson 2015) [with the notable exception of magnetars, where the decaying magnetic field may provide an internal heat source (Beloborodov & Li 2016)], while NSs in binaries (Perego, Bernuzzi & Radice 2019), post-merger NS remnants (Oechslin, Janka & Marek 2007; Kastaun et al. 2017), and especially accreting pulsars (Potekhin et al. 2003; Beloborodov & Li 2016; Camelio et al. 2021) can have spatially dependent temperature profiles that span several orders of magnitude. The resultant position-dependent thermal pressure makes the ratio between the effective adiabatic index of the equilibrium and that for the perturbation a function of position.

For mature NSs, the temperature is typically low enough to allow the appearance of solid crust, superfluid core, and superconductivity of protons. Taking the multilayer complexity in full, $g$ modes can be distinguished into two classes, viz. core and crust $g$ modes, depending on the configuration of the rendered motions (McDermott et al. 1985; McDermott, van Horn & Hansen 1988). For instance, the radial motion caused by a core $g$ mode will be viscously quenched at the crust–core interface, leading to only slight perturbations in the crust. The mode frequencies for both classes will acquire some modifications by the inclusion of superfluidity, which tends to increase the frequencies of crust $g$ modes. None the less, we do not take the multilayer influences on the spectrum into account as the first step to reveal the trifurcation of EOS in terms of $g$ modes.

It has been shown that the $f$-mode frequency of a given star is largely determined by the square root of its mean density (Andersson & Kokkotas 1998; Krüger & Kokkotas 2020),

$$\rho_{\rm mean} = \frac{M}{\frac{4}{3}\pi R^3}, \tag{5}$$

which is $\sim$0.33 for typical values of mass and radius of NSs, viz. 1.4 $M_\odot$ and 10 km, in the units adopted here. We find a similar empirical relation but augmented with a dependence on stratification, given by

$$f_{\rm g}/\sqrt{\delta} \propto \rho_{\rm mean}^{(1-\varsigma)/2}, \tag{6}$$

for quadrupolar ($l = 2$) $g_1$, $g_2$, and $g_3$ modes in stars having mass larger than 1 $M_\odot$ for a variety of EOSs. Here, $\varsigma$ is the fitting parameter, which varies for different EOSs, while the proportionality constant depends on the mode quantum numbers for fixed overtone numbers ($g_1$, $g_2$,...) as well as the EOS. However, despite this dependence, we find that it behaves in a quantitatively similar manner between different EOS groups (see Section 2.3). Furthermore, the fact that $g_1$ to $g_3$ modes follow the same relation indicates that the ratio between their frequencies can be approximated by a constant; e.g. we find that

$$f_{\rm g_2}/f_{\rm g_1} \simeq 0.68 \tag{7}$$

for every EOS considered.

Assuming single-component fluid NSs, the justification for $\delta$ introduced above may then be obtained by separating the contribution of the thermal pressure,

$$p^{\rm x}_{\rm th} = \frac{\pi^2}{6}\frac{n_{\rm x}}{E^{\rm x}_F}(kT)^2, \tag{8}$$

in the perturbation equations used to solve for QNMs, where x = {n, p, ...} runs over the different constituents of the fluid. Here, $p^{\rm x}_{\rm th}$ represents the thermal pressure provided by the species x, whose Fermi energy is $E^{\rm x}_F$. In particular, the thermal pressure contributes to the linearized equations of the radial and tangential displacements [see equations (B3) and (B4) of Krüger et al. (2015)], which replace the term $\gamma p$ for NSs, where thermal gradients are absent, with [see equation (B5) of Krüger et al. (2015)]

$$\Gamma p := \gamma p + \sum_{\rm x}\frac{\partial p^{\rm x}_{\rm th}}{\partial n_{\rm x}} n_{\rm x} = \gamma(1+\delta)p, \tag{9}$$

where

$$\delta = \left[\frac{k^2\pi^2}{6}\sum_{\rm x}(E^{\rm x}_F)^{-1}\right] T^2 \tag{10}$$

is proportional to $T^2$. Although this implies that equation (6) can be translated to

$$f \propto \rho_{\rm mean}^{(1-\varsigma)/2} T \tag{11}$$

if the NS is isothermal, such a parametrization needs to be justified for an inhomogeneous temperature profile. To evaluate the reliability of equation (11) for a NS with more general temperature distribution, we have compared the mode frequencies in isothermal stars with the cases of stars with radial temperature profiles that fall by one to two orders of magnitude from centre to the surface by using the code described in Krüger et al. (2015). In particular, we solve for the frequencies of the $g_1$ mode for a particular stellar model with the following temperature profiles (in the unit of $K$): (i) isothermal with $\log T = \{10, 9.5, 9\}$; (ii) falling temperature by an order of magnitude as approaching the surface from the temperature at the centre being $\log T = \{11, 10\}$; and (iii) falling temperature by more than one order of magnitude for a central temperature of $\log T = \{11, 10.8, 10.6, 10.4, 10.2, 10\}$ and a fixed surface temperature $\log T = 9$. The falling temperature profiles are such that the temperature decreases linearly with the radius on a logarithmic temperature scale. As such, those profiles are highly artificial and given the multitude of different cooling and heating mechanisms operating inside a NS it would be difficult, and beyond the scope of this work, to reproduce a realistic temperature profile. However, as we argue below, the most important part of the temperature profile is only that close to the surface of the star and since we are mostly interested in a qualitative understanding of temperature-related effects, such a simply constructed temperature distribution suits our needs.

We found that the spectrum of NSs with the same surface temperature differs only slightly among the above three scenarios, indicating that, to leading order, the QNM spectrum is unaffected by the temperature gradient except in extreme circumstances [cf. the case of proto-NSs discussed by Torres-Forné et al. (2019); see also Sotani, Takiwaki & Togashi (2021)]. This finding makes sense as the

thermal pressure $p_{\rm th}$ is a function quadratic in the temperature; being causal for the buoyancy, it can compete with the static pressure, which grows substantially towards the centre of the star, only in the outer regions of the star and, hence, the surface temperature is the primary quantity to determine the $g$-mode spectrum of a star. This argument also tells us that the shell below the surface that impacts the $g$-mode spectrum grows in depth with increasing surface temperature. We do observe this effect: Linearity between $f$ and $T$ was observed for $T \lesssim 10^{10}$ K, and a more complicated pattern arises only for $T > 10^{10}$ K.

### 2.2 Tidal heating

For stars within compact binaries permitting 'tidally neutral $g$ modes' (see Appendix A for details), mode-related tidal effects are dominated by the non-resonant $f$ mode until merger. Resonant $g$ modes may contribute to the tidal effects comparable to $f$ mode for stars whose $g$ modes are tidally susceptible; e.g. the produced stress may cause crust yielding (Passamonti, Andersson & Pnigouras 2021) and the heating via shear viscosity may be as important as that resulting from the $f$ mode (Lai 1994). For the latter heating process, we find that the energy absorbed into the star via $g$ modes up to $g_{16}$ mode[1] can amount to $E_{\rm kin} \sim 10^{43}$ erg for binaries consisting of identical components, where the kinetic energy of each mode acquired during the tidal excitation is consistent within a factor of $\sim$5 with the stationary-phase-approximated formula [see equation (6.11) in Lai (1994)],

$$E_{nl} \simeq 9.70 \times 10^{42}\text{erg} \times \left(\frac{\rho_{\rm mean}}{0.49}\right)^{-1} \left(\frac{f_{nl}}{100\ \text{Hz}}\right)^{1/3} \left(\frac{Q_{ln}}{10^{-5}}\right)^{2}. \quad (12)$$

A portion of the mechanical energy will be converted into thermal energy via viscosity (Lai 1994; Sherf 2021) mainly provided by lepton shear viscosity when $T < 10^9$ K [cf. fig. (1) of Andersson, Comer & Glampedakis (2005) and also Kolomeitsev & Voskresensky (2015)] and chemical reactions, such as direct or modified Urca processes (Arras & Weinberg 2019). To set an upper limit for the heating effect, we assume that the whole energy budget deposited by the finite series of $g$ modes is converted into thermal energy through the aforementioned channels; consequently, NSs will be heated up to a temperature

$$T \simeq 4.7 \times 10^{6} \left(\frac{E_{\rm kin}}{10^{43}\ \text{erg}}\right)^{1/2} \text{K}, \quad (13)$$

by equating the dissipated energy to the heat content $U$ of NSs (Lai 1994; Arras & Weinberg 2019), which related to the averaged temperature over the core via [equation (8.28) in Lai (1994)]

$$U \simeq 4.5 \times 10^{45} \left(\frac{T}{10^{8}\ \text{K}}\right)^{2} \text{erg}. \quad (14)$$

Although $f$-mode excitation may also extract orbital energy thus attributing to the tidal heating, the amount of the kinetic energy is estimated to be comparable to the gross value of $g$ modes (Lai 1994). The square root dependence of the temperature on the kinetic energy, as expressed in equation (13), therefore indicates that the resultant temperature will be of the same order, which is cold enough not only for the appropriateness of our implementation of cold EOS, but also for the justification of $\delta \propto T^2$.

We note that the above temperature may be too cold to admit $g_1$ mode with a frequency of $\gtrsim$100 Hz since we estimate the heating effect for non-spinning NSs. For the rotating stars, $r$ modes, even $f$ mode, may undergo a period of resonance (Ho & Lai 1999; Lai & Wu 2006), thus soaking more energy in expense of orbital one to heat further the star.

### 2.3 Three groups

In equation (6), the exponent is determined as follows: for a certain value of $\varsigma$, a least-squares fitting is applied to $f_{\rm g}/\sqrt{\delta}$ and $\rho_{\rm mean}^{(1-\varsigma)/2}$, from which we calculate the correlation coefficient; we then define the parameter to be the value of $\varsigma$ that maximizes the correlation coefficient. We collate the fitting parameters $\varsigma$ in Table 1. We see that $\varsigma$ can be divided into three ranges (with a few outliers): $\gtrsim$0.2 (*Group I*; first column), $\sim$0–0.2 (*Group II*; second column), and $\lesssim$0 (*Group III*; final column). The width of the 95 per cent confidence interval of $\varsigma$ for each EOS is $\lesssim$0.01, indicating that the grouping presented here is statistically sharp. The three divisions intriguingly correspond to EOS consisting of only hadronic matters that can support heavy stars of mass $\gtrsim$2.12 $M_\odot$ or more (Group I), those that cannot (Group II; $\lesssim$ 2.07 $M_\odot$ or less), and EOS involving phase transitions leading to either hyperon condensation or quark deconfinement (Group III). We note that the considered EOS of Group III cannot support stars much heavier than $\sim$2 $M_\odot$. The few two peculiar EOSs are ENG and PAL6; the first is an outlier of *Group I* with $\varsigma < 0.2$, while the latter EOS is an exception of *Group III* since it has a positive $\varsigma$ and the matter consists of hadrons. This slight mixing between Group III and the others is not entirely surprising, since first-order transitions in EOS that only support relatively light stars will not play a big role. In general, we see that the mass–radius relation is 'flattened' with decreasing $\varsigma$, and becomes a one-to-one mapping when $\varsigma \lesssim 0.2$ except for the Group I EOS ENG and the Group III EOS ALF2. A natural question about this grouping is whether they are classified by 'softness'? While this may be a general trend, it is not absolute since, for example, the stiffest EOSs are MS1 and MS1b, which are in Group I, while members in Group III tend to be stiffer than those in the other two groups.

We illustrate the nature of the groups by plotting the $g$-mode frequency for a fixed $\delta$ as a function of (the square root of) $\rho_{\rm mean}$ in Fig. 2, where the different markers are used to indicate the different correlations between the range of $\varsigma$. For instance, EOSs for which $\varsigma \gtrsim 0.2$ (Group I) are represented by solid circles. One observes that the $g$-mode frequencies even of very stiff EOSs like MS1 and MS1b align well [in the sense of equation (6)] with other EOSs of Group I, especially when the difference in the radius for NSs with a fixed mass among these EOSs can be as large as 1.5 times (between WFF1 and MS1). This observation is similar for respective members of the other two groups, clearly indicating that global parameters associated with the EOS are not the only factor in contributing to $g$ modes. On the other hand, it has been shown that $g$ modes in proto-NS following a core collapse, which may be detected in the near future by third-generation detectors (Ott et al. 2006; Bizouard et al. 2021), tend to obey a universal relation, and there is no obvious partition (see e.g. fig. 2 in Torres-Forné et al. 2019). The absence of grouping in proto-NSs may arise for two reasons: (i) they have very high temperature, likely indicating that they are thermally stratified to the degree that $\delta \gtrsim 1$ (for which the correlation we find between $T$ and $\delta$ may no longer hold), and thus the situation may be different from cold NSs (see Section 2.3 for the discussion on valid range

[1] We note that $\sim$80 per cent of the energy budget is deposited by $g_1$–$g_5$ modes. In addition, there is a caveat that high-order $g$ -modes, whose oscillatory periods are smaller than the time-scale of the involved reaction rate, are likely swept off from the spectrum (Andersson & Pnigouras 2019).

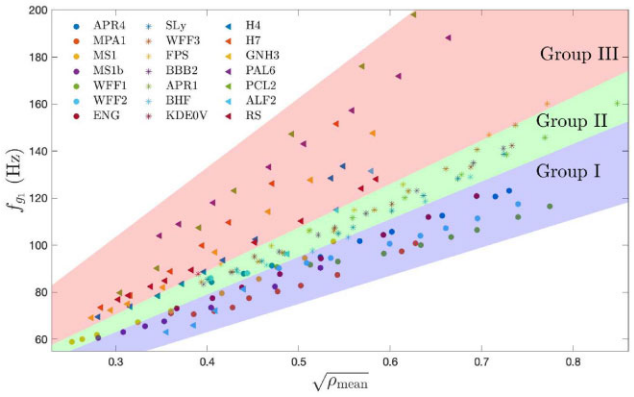


**Figure 2.** $g$-mode frequency for $\delta = 0.005$ as a function of the square root of the mean density, $\sqrt{\rho_{\rm mean}}$, for each of the EOSs under study. The circles represent those models drawn with solid line in Fig. 1, the asterisks pair the dashed-line EOS, and the triangles correspond to the dash–dot EOS.

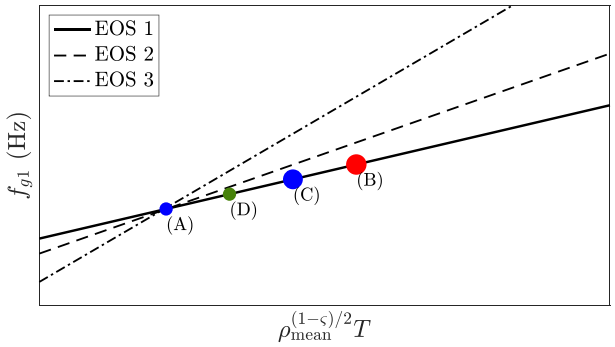


**Figure 3.** Symbolic *g-space* (see the main text for the definition) for three EOSs – one from each group, and four hypothetical observations. The chosen EOS trifurcates around a certain point in the space, so that all three branches can explain observation (A). However, suppose that, for demonstration purposes, Group I (EOS 1) governs NSs from different systems (and thus passes through each observation). The member(s) in Group II (EOS 2) can fit the observation in system (A), and may be able to explain observation (D) depending on the error bars of the measurement, though are incapable of matching the data for (C) or (B). The Group III case (EOS 3), by contrast, is unable to explain any observation except (A).

of the introduced parameter $\delta$); and (ii) the EOS families that have been previously considered in this context may incidentally belong to the same branch. Although beyond the scope of this paper, it would be worth revisiting $g$-mode studies in proto-NS with a wider EOS library to investigate these points.

Cold NSs with similar bulk properties display universal relations between the $f$, $p$, and $w$ modes, indicating that the particulars of internal structure do not impact these modes much (Andersson & Kokkotas 1998; Krüger & Kokkotas 2020; Benitez et al. 2021; Sotani & Kumar 2021). However, the compositional content of NSs, which is to a large extent unknown, will substantially affect the $g$-mode spectrum. The uncertainty in the internal physics, on top of the various methods and/or assumptions adopted to model the nuclear interactions, leads to the richness in variations of EOS candidates; the grouping we observe therefore indicates that microphysical considerations can be broadly categorized into three channels, each leading to a family of $g$ modes in Fig. 2. For instance, the constituents in the core depend on their evolution track since certain cooling/reaction channels have density-dependent activation thresholds. In addition, atomic abundances in the crust may vary from system to system, depending on their birth site (Kowalska-Leszczynska et al. 2015; Woosley, Sukhbold & Janka 2020). Crustal variations are unlikely to considerably modify the *core* $g$-mode spectrum however, and thus would not be responsible for the grouping.

Due to the limited precision of any given observation, it is likely that we can only distinguish one family of EOS from another rather than two EOSs in the same family. If it happens that there are two phenomena caused by $g$ modes, and these are found to reside in different groups, it might imply that the NSs have followed a different evolutionary track as far as the EOS is concerned. None the less, if we assume that a certain functional EOS applies to NSs in different systems, such as binaries and long-lived remnants of mergers, these compact objects will belong to the same line (solid line in Fig. 3) describing the $g$-mode frequency as a function of $\rho_{\rm mean}^{(1-\varsigma)/2}T$, just at different stages. Defining the $g$-space as the set consisting of the $g_n$-mode frequencies that can be possessed by at least one star with this EOS, we indicatively draw the $g_1$-space in Fig. 3 for EOSs 1–3; each belongs to groups I–III, respectively. The observations of several events can therefore be incorporated to provide a mutual constraint on the EOS candidates (see below) but in a manner that is distinct from Bayesian analyses, where various observations shape the prior of the parametrization of EOS differently to gradually reduce the viable region for EOS candidates (see e.g. Miller, Chirenti & Lamb 2019; Raaijmakers et al. 2020, 2021). We note that in a formal Bayesian analysis, this common EOS assumption will shape the (informative) prior of model parameters differently than the situation when the assumption is absent, thus affecting the statistical inference (Kastaun et al. 2017).

As an illustrative example, we consider the particular combination of systems; (A) represents a NS in a binary undergoing the inspiral, (B) stands for a newly born NS from merger after the temperature has dropped sufficiently to validate equation (11) and differential rotation has largely stabilized,[2] and (C) denotes an old, long-lived remnant from a NS merger, with finally a less-compact version in (D) (see also below). Each type of observation from different NSs is designated as a point in the space spanned by $f_{\rm g_1}$ and $\rho_{\rm mean}^{(1-\varsigma)/2}T$, and the solid line connecting these three points indicates a hypothetical case where one EOS 'branch' satisfies (A)–(D). We see that the lines for different groups diverge, but with only one measurement point (A), one cannot tell which line it is unless some additional observations are available; branches can be ruled out by incorporating the multistage information across (A) to (C), depending on the relative error bars on the measurements. None the less, we emphasize that the above analysis surrounding Fig. 3 does not necessarily reflect the reality. Instead, it is simply a demonstration of the idea.

In order to map a certain system on to the $g$-space, the mean density, which implies we are able to probe the mass and radius to a certain extent, and volume-averaged temperature, must be known. Although certain constraints can already be set by the simultaneous determinations of the mass and the radius by, e.g. marking a valid region on the mass–radius diagram for EOS, there will still be a

[2]A NS remnant from a merger forms in a differentially rotating state, and is likely to be highly magnetized due to the Kelvin–Helmholtz instability occurring at the shear boundary formed upon the contact of the two progenitors (Kiuchi et al. 2015). The non-uniform rotation will wind the field lines and is thought to produce a turbulent viscosity however, which diffuses the angular momentum from the fast to slow regions, thus unifying the rotation profile (or at least confining it to vary only along flux lines in accord with the axisymmetric Ferraro theorem) in just a few tens of milliseconds (Duez et al. 2004; Fujibayashi et al. 2018).

bunch of EOSs surviving such restriction if the radius has even small error bars (e.g. Lindblom 1992; Weih, Most & Rezzolla 2019). Information from the $g$-mode frequency can, in such cases, provide additional constraints of a different flavour. Considering a NS with a canonical mass of 1.5 $M_\odot$ and a radius of 11–12 km (corresponding to $\sqrt{\rho_{\rm mean}} = 0.46$–$0.52$), for example, several members of groups I and II are adequate in terms of the mass and the radius observations, viz. APR4, MPA1, WFF2, SLy, WFF3, FPS, KDE0V, and BBB2 (though considering higher mass or more compact stars reduces the pool; Weih et al. 2019). Some of these EOSs will be ruled out if $f_{g_1}$ can be acquired; for instance, $f_{g_1} \lesssim 80$ Hz will exclude ones belonging to Group II, thus making a 62.5 per cent reduction in the aforementioned EOS candidates (see Fig. 2).

To observe a given system on the $g_1$-space, there must be some phenomena attributed to its $g_1$ mode. The candidate systems allowing for $g$-mode measurement will be discussed in Section 4, where we consider electromagnetic precursor flares prior to merger (Section 4.1) and QPOs in the X-ray light curves of accreting millisecond X-ray pulsars (AMXPs; Section 4.2).

## 3 UNIVERSAL RELATIONS

In addition to the EOS-dependent relation (6) (or equation 11), we provide three EOS insensitive relations bearing $g$-mode frequencies to $f$-mode frequency, dimensionless tidal deformability $\Lambda$ (Section 3.1), and the central speed of sound (Section 3.2), respectively. These relations offer extra means not only to distinguish EOS groups, but also to extract information on the properties of NSs from gravitational- and/or electromagnetic-radiation observations. We consider hereafter only EOSs of groups I and II, pondering that these are favoured by precursor events (see the discussion near the end of Section 4.1).

### 3.1 Gravitational waves

When analysing a high-signal-to-noise gravitational waveform, the chirp mass,

$$\mathcal{M} = \frac{(M_1 M_2)^{3/5}}{(M_1 + M_2)^{1/5}}, \tag{15}$$

of the system can be determined to a relatively high precision since it enters the phase evolution at the lowest post-Newtonian (PN) order (Peters & Mathews 1963; Cutler & Flanagan 1994). Although not with the same level of accuracy, the symmetric mass ratio,

$$\eta = \frac{M_1 M_2}{(M_1 + M_2)^2}, \tag{16}$$

can also be obtained by exploiting its PN-order contribution to the GW phase [see e.g. equation (32) in Kokkotas, Królak & Tsegas (1994)]. Therefore, the individual masses $M_1$ and $M_2$ can be estimated from $\mathcal{M}$ and $\eta$. In addition, a detailed extraction of the phase shift $\delta\Psi = \delta\Psi_{\rm eq} + \delta\Psi_{\rm dyn}$ may shed light on both equilibrium and dynamical tidal effects (Pratten, Schmidt & Hinderer 2020), for which the mutual, dimensional tidal deformability (Hinderer et al. 2010; Abbott et al. 2017),

$$\tilde{\Lambda} = \frac{16}{13}\frac{(M_1 + 12M_2)M_1^4\Lambda_1 + (M_2 + 12M_1)M_2^4\Lambda_2}{(M_1 + M_2)^5}, \tag{17}$$

is the agency of the former, and the latter is mainly produced by the late stage growth of $f$ mode (Hinderer et al. 2016; Schmidt & Hinderer 2019; Steinhoff et al. 2021). Here, $\Lambda_{1(2)}$ is the tidal deformability of the primary (companion). With observables $\mathcal{M}$, $\eta$, and $\tilde{\Lambda}$, we get

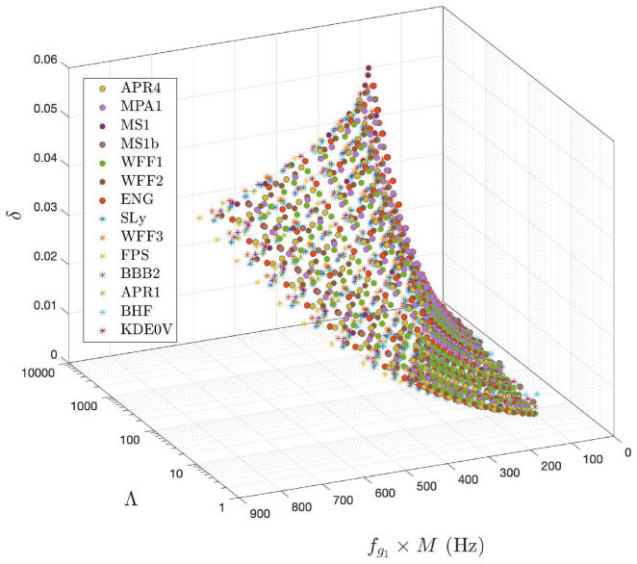


**Figure 4.** Three-dimensional universal relation among mass-scaled $g_1$-mode frequency, the tidal deformability, and the stratification for EOS in groups I and II.

a relation for $\Lambda_1$ and $\Lambda_2$, and the masses $M_1$ and $M_2$ though with certain error. However, the uncertainty of EOS involved in such analysis has a ramification on measuring stellar properties, which can be mitigated by implementing EOS-insensitive relations.

Although there are several universal relations in hand, most of them pertain to properties of individual NSs, such as the I–Love–Q relation (Yagi & Yunes 2013), and can only become useful when the mass ratio between two components of a binary is provided. We therefore are seeking a scheme to obtain the properties of individual star from the observables without the a priori input of the mass ratio. We illustrate that with $g$-mode frequency obtained from electromagnetic observations, e.g. the timing of precursors (Kuan et al. 2021b), such methodology can be established.

In Fig. 4, we show a universal sheet associating the $g_1$-mode frequency, the tidal deformability, and the stratification. The caveat of this relation is that $\delta$ may be identified with different temperatures for different EOSs; therefore, it may not be useful even when the temperature can be observed or estimated. To circumvent this dilemma, we can count on an additional information of $g_2$ mode, whose frequency is linearly correlated with that of $g_1$ mode through

$$f_{g_1} = a_0 + a_1 f_{g_2}, \tag{18}$$

where the coefficients $a_0$ and $a_1$ are found to be rather insensitive with $\delta$, e.g. $a_0 = 4.3162$ and $a_1 = 0.620$ for $\delta = 0.005$, and $a_0 = 5.7221$ and $a_1 = 0.623$ for $\delta = 0.01$. None the less, the difference $f_{g_1} - f_{g_2}$ depends strongly on $\delta$, thus limiting $\delta$ to a certain range if the frequencies of these two modes can be observed. One of the possible scenario, where such detection is plausible, is precursor flares of SGRBs, and we will give a concrete example in Section 4.1 of limiting the range of $\delta$ via the frequency difference.

Denoting $\delta_5 = \delta/0.005$, we plot as the solid line the universal behaviour,

$$\frac{f_{g_1}}{100\ {\rm Hz}}\frac{M}{\sqrt{\delta_5}} = -48.641 + 70.782\left(\frac{f_{\rm f}}{1\ {\rm kHz}}R\right) - 34.426\left(\frac{f_{\rm f}}{1\ {\rm kHz}}R\right)^2 + 5.695\left(\frac{f_{\rm f}}{1\ {\rm kHz}}R\right)^3, \tag{19}$$

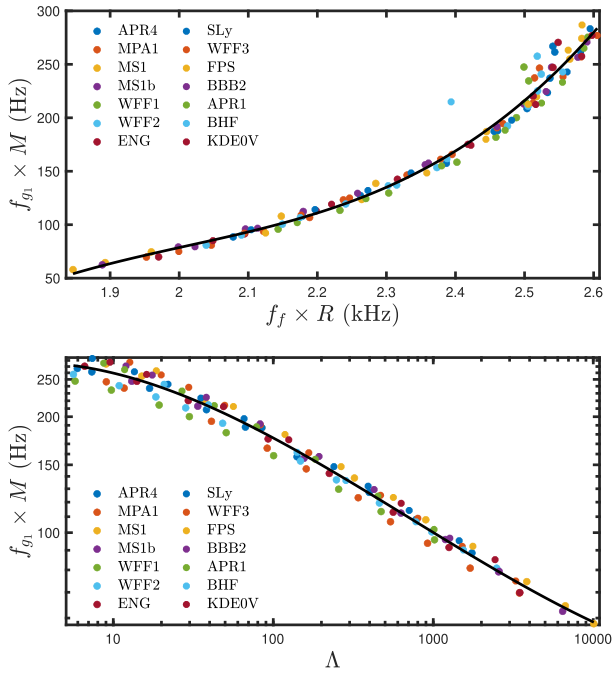


**Figure 5.** Universal relations for the EOS considered here: the mass-scaled $g_1$-mode frequency as a function of the radius-scaled $f$-mode frequency (top panel), and the compactness-scaled $g_1$-mode frequency as a function of $\Lambda$ (bottom panel).

relating the radius-scaled $f$-mode frequency and the mass-scaled $g_1$-mode frequency in the top panel of Fig. 5. The above equation suggests that the quantity of $g_1$-mode frequency divided by $\sqrt{\delta_5}$ depends on the global quantities of the star given $f$-mode frequencies strongly correlated to the mean density, which matches to the indication of equation (6). Although the relation is valid for, as far as we have checked, $0.001 \leq \delta \leq 0.05$, we present only the results for $\delta_5 = 1$ (coloured dots) in Fig. 5 for ease of presentation. In the bottom panel, we plot a certain section of the sheet in Fig. 4, which shows a bearing on dimensionless tidal deformability via the relation (solid line)

$$\log\left(\frac{f_{g_1}}{100\ \mathrm{Hz}}\frac{M}{\sqrt{\delta_5}}\right) = 0.411 + 0.106\log\Lambda - 0.126(\log\Lambda)^2 + 0.015(\log\Lambda)^3. \quad (20)$$

Here, the individual quantity $\Lambda$ must not be confused with the observed mutual deformability $\tilde{\Lambda}$. Additionally, a relation between the mass-scaled $f$-mode frequency and $\Lambda$ was proposed by Chan et al. (2014), which reads

$$\log\left(\frac{f_{\mathrm{f}}}{\mathrm{kHz}}M\right) = 0.814 - 0.050(\log\Lambda) - 0.035(\log\Lambda)^2, \quad (21)$$

for the EOS considered here. We note that equations (19) and (20) are invertible maps over the domains of interest, suggesting a one-to-one relation connecting $f_{\mathrm{f}} \times R$ and $\log\Lambda$. Despite the fact that inverting these two equations and then using the common factor $f_{g_1} \times M$ to parametrically fit $f_{\mathrm{f}} \times R$ and $\log\Lambda$ can establish such a relation, we instead directly establish a fitting formula between the data, given by

$$\log\left(\frac{f_{\mathrm{f}}}{\mathrm{kHz}}R\right) = 0.409 + 0.013(\log\Lambda) - 0.013(\log\Lambda)^2, \quad (22)$$

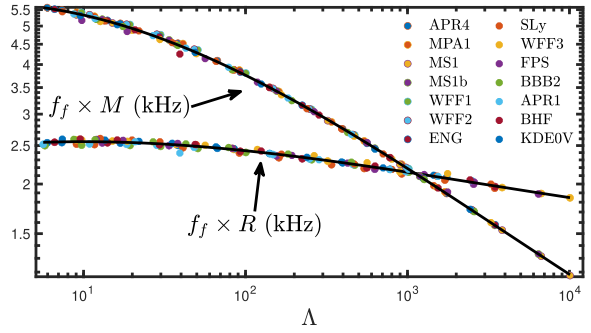


**Figure 6.** Universal relations established in Chan et al. (2014) relating the mass-scaled $f$-mode frequency to $\Lambda$, and relation (22) associating the radius-scaled $f$-mode frequency to $\Lambda$, for the EOS considered here.

which can be viewed as an equivalent of equation (21), and both are shown in Fig. 6. Combining above relations (20) and (21), the ratio between the frequencies of $f$ and $g_1$ modes can be expressed as a function of $\Lambda$, given by

$$\log\left(\frac{f_{g_1}/\sqrt{\delta_5}}{f_{\mathrm{f}}}\right) = -1.403 + 0.156(\log\Lambda) - 0.091(\log\Lambda)^2 + 0.015(\log\Lambda)^3. \quad (23)$$

The aforementioned relations are powerful in rephrasing observables in terms of unobservable but important quantities. Stipulating that we get individual masses from the measurements of the chirp mass and the symmetric mass ratio (see below), and the frequency of $g_1$ mode of the primary from, e.g. precursor observations, we can deduce the individual deformability $\Lambda_1$ from equation (20). Subsequently, equation (21) translates the mass into $f_{\mathrm{f}}$ of the primary, which then returns the radius $R_1$ via equation (19). If we also have knowledge of the mutual tidal deformability, the companion's individual deformability $\Lambda_2$ can be obtained, which, together its mass, gives the secondary's $f$-mode frequency via equation (21). Accordingly, equation (23) provides an estimate on the $g_1$-mode frequency of the companion, which, combined with aforementioned companion properties, returns the radius through equation (19).

In reality, the measurements of $\eta$, $\tilde{\Lambda}$, and $\mathcal{M}$ all come with error, though the uncertainty on $\mathcal{M}$ is typically smaller than the others (see e.g. Cutler & Flanagan 1994; Królak, Kokkotas & Schäfer 1995). On top of the above, an uncertainty of $\sim$10 Hz in $f_{g_1}$ could also be expected, which effectively translates into error bars for the temperature. All these errors will be reflected in the predictions of equations (19)–(23). As a specific example, we assume $f_{g_1} = 100 \pm 10$ Hz, and adopt the chirp mass $\mathcal{M} = 1.167$ with $\eta = 0.242$–$0.25$ and the mutual tidal deformability $\tilde{\Lambda} = 200$–$800$ of a GW170817-like binary (e.g. De et al. 2018; Abbott et al. 2019) in Fig. 7, where the derived tidal deformability of the primary (top panel) and the companion (bottom panel) is plotted for $0.005 \leq \delta \leq 0.01$. Here, the blue lines represent the stratification $\delta = 0.005$, typical for mature NSs in coalescing binaries (e.g. Lai & Wu 2006), while the red lines depict a relatively large $\delta = 0.01$, which may be realized in heated stars (achieved, e.g. through close, tidal interaction or accretion). The mid-point, $\delta = 0.0075$, is plotted as orange lines. The region bounded by the lines encapsulates the possible range. We first look at the influence of $\delta$ by taking, for instance, $\eta = 0.25$, $\tilde{\Lambda} = 800$, and $f_{g_1} = 100$ Hz. We find for the primary $\Lambda_1 = 692.72^{+552.47}_{-389.44}$, $R_1 = 1.55^{+0.42}_{-0.44}$, and $f_{\mathrm{f}} = 1829.31^{-256.62}_{+394.23}$ Hz, while $\Lambda_2 = 907.28^{-552.47}_{+389.44}$, $R_2 = 1.26^{-0.20}_{+0.09}$, and $f_{\mathrm{f}} = 1708.63^{+454.48}_{-152.89}$ Hz for

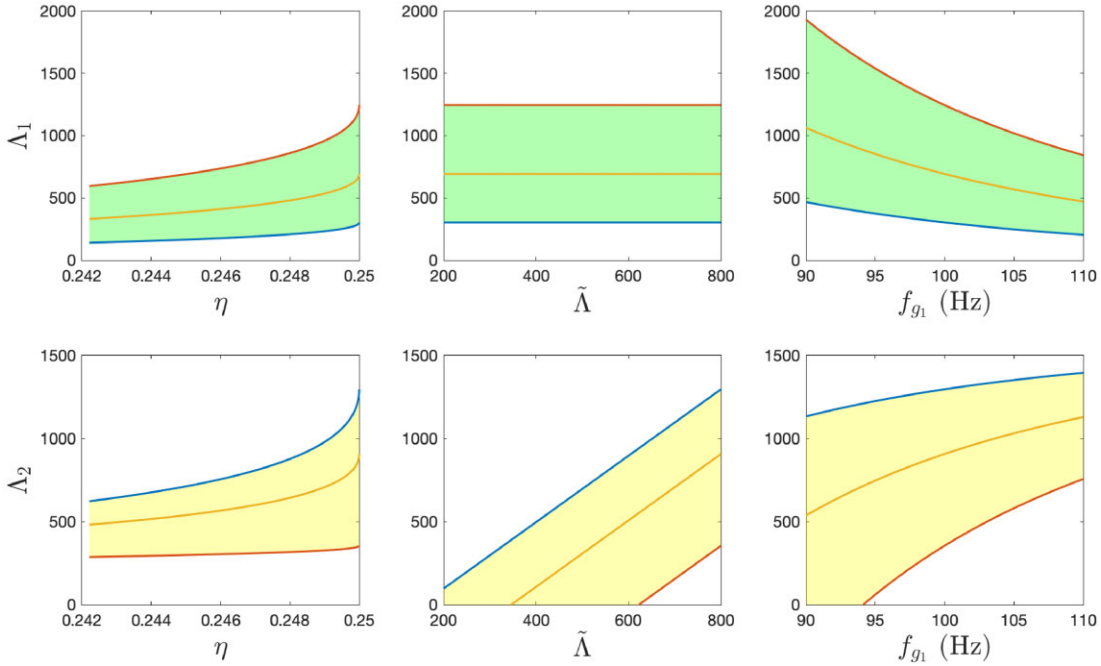


**Figure 7.** Inferred, individual tidal deformability of the primary (top panel) and the companion (bottom panel), determined via equations (19)–(21), using a fixed value of $\mathcal{M} = 1.167$. The width of each band is due to an assumed uncertainty in the stratification $\delta$. Three specific $\delta$ are plotted as solid lines on the shaded area: $\delta = 0.005$ (blue lines), typical for mature NSs, $\delta = 0.01$ (red lines), which may be relevant if the star is heated by some processes (see the main text), and a mid-point stratification $\delta = 0.0075$ (orange lines). In each cell, one of $\eta$, $\tilde{\Lambda}$, and $f_{g_1}$ is varied (as per the horizontal axis) while the other two are fixed at $\eta = 0.25$, $\tilde{\Lambda} = 800$, and $f_{g_1} = 100$ Hz.

the companion, where the values correspond to $\delta = 0.0075$ with the superscript (subscript) associated with $\delta = 0.01$ ($\delta = 0.005$).

Among the uncertainties in $\mathcal{M}$, $\eta$, and $\tilde{\Lambda}$, the latter is the most significant since it is extracted from fifth PN-order effects in the gravitational waveform (Flanagan & Hinderer 2008; Hinderer et al. 2010), which leaves a smaller imprint than the Newtonian-order parameter $\mathcal{M}$ and 1PN parameter $\eta$. Although in our scheme, the large uncertainty in the mutual tidal deformability does not alter the inference of the parameters of the primary if the $g_1$-mode frequency and the masses of the NSs are well constrained (see e.g. the second column in the top panel of Fig. 7), the inferred properties of the companion are affected considerably. For example, $\Lambda_2 = 97$–$1297$ and $R_2 = 0.86$–$1.36$ correspond to this error given $\eta = 0.25$, $f_{g_1} = 100$ Hz, $\delta = 0.005$, and the above parameters of the primary. Physically speaking, this is because we attribute a $g$ mode to the primary and not the secondary, so that less information is obtained about the latter using the formulae derived here. In addition, the predictions are sensitive to $\eta$ and $f_{g_1}$ as illustrated in Fig. 7, where the inferred tidal deformability can drop by 50 per cent from symmetric case ($\eta = 0.25$) to a mildly asymmetric case with $\eta = 0.242$. On the other hand, they can increase by a factor of 2 if the $g_1$-mode frequency of the primary is $f_{g_1} = 90$ Hz instead of 110 Hz.

Although the individual masses $M_1$ and $M_2$ can be determined by the chirp mass and the symmetric mass ratio measurements, with an error mainly due to the latter (see e.g. sections 5 and 6 of Kokkotas et al. 1994, for a discussion), the radii of constituents cannot be easily constrained. The $g$-mode methodology, however, can additionally determine the radii of binary members with high accuracy if the temperature is modest. As the radius of NSs with a mass of 1.4 $M_\odot$ still spans a range of 11–13 km for EOS candidates that pass the observations (e.g. Capano et al. 2020; Dietrich et al. 2020; Landry, Essick & Chatziioannou 2020; Pang et al. 2021), such a novel way

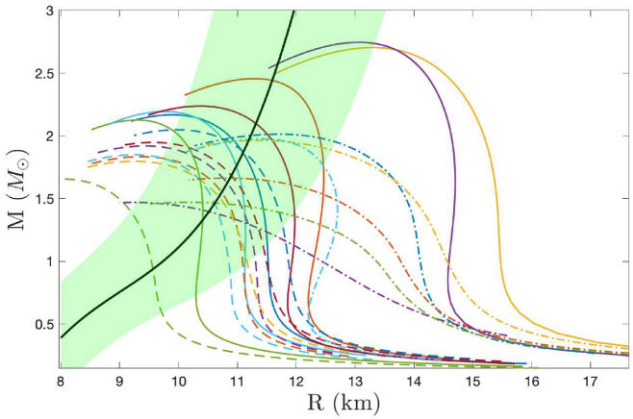


**Figure 8.** The curves same in Fig. 1 overlapped with equation (19). The solid line stands for the case with $f_f = 2.2$ kHz and $f_{g_1} = 100$ Hz, and the shaded area corresponds to the range of $f_f = 2$–$2.4$ kHz and $f_{g_1} = 80$–$120$ Hz.

to measure the radius may therefore constitute a valuable tool in whittling down the pool of currently viable EOSs.

On top of this arguably already executable application of universal relations, we speculate on the possibility of detecting, though indirectly, the $f$-mode frequency from the accumulation of phase, $\delta\Phi_{\rm dyn}$. This is expected to be plausible with detectors in the near future. In particular, $f_f$ of the progenitors of GW 170817 may be determined to within tens of Hz with the Einstein Telescope (Pratten et al. 2020).

The determination of $f_f$ has a double dose of implications. First, incorporation of equations (19)–(21) results in an 'on-shell' (physically realizable) condition of $M(R)$ if $f_f$ and $f_{g_1}$ are provided. In Fig. 8, we overlap the 'on-shell' $M(R)$ to the mass-to-radius diagram

of the EOS considered here for the typical values of $f_{\rm f} = 2$–$2.2$ kHz and $f_{\rm g} = 80$–$120$ Hz. Here, the solid line corresponds to $f_{\rm f} = 2$ kHz and $f_{\rm g_1} = 100$ Hz. Secondly, we can know simultaneously the mean density due to its universal relation with *f*-mode frequency (Chan et al. 2014; Krüger & Kokkotas 2020). According to the derived mean density and the $g_1$-mode frequency, we can represent the NS on Fig. 2, and thereby sift the branch of EOS for this system. We note that even for binaries without precursors, $f_{\rm g_1}$ can be determined through equation (20) if the tidal deformability $\Lambda$ is measured.

Another scenario where these EOS-insensitive expressions are particularly helpful is black hole–NS binaries since the individual tidal deformability equals to the mutual one, which is an observable, thus activating the equations (20)–(23) without the additional processing translating observables to $\Lambda$.

### 3.2 Speed of sound

The measurement of $g_1$ mode can be translated into the central sound speed of the equilibrium via the strong correlation,

$$\frac{f_{\rm g_1}/\sqrt{\delta_5}}{100\ {\rm Hz}}\left(\frac{v_{\rm s}}{R}\right) = 0.124 - 0.296\rho_{\rm mean}^{0.5} + 1.685\rho_{\rm mean} + 1.442\rho_{\rm mean}^{1.5}, \quad (24)$$

shown as the solid black line in Fig. 9. Given that the stiffness of an EOS can be characterized by the maximum sound speed (Van Oeveren & Friedman 2017), this central value may be informative enough for shedding light on the stiffness of the EOS since the sound speed culminates at the centre. The stiffness of EOS affects the bulk properties of NSs, such as the maximum mass that is supportable with the EOS (Moustakidis et al. 2017; Zhang, Wen & Chen 2019), and the tidal deformability (Van Oeveren & Friedman 2017; Kanakis-Pegios, Koliogiannis & Moustakidis 2020); therefore, the constraint on the stiffness may be translated to either the upper or the lower bound for the sound speed. For instance, the lower bound of sound speed should be $\sqrt{0.6}$ if the secondary of the binary hosting GW 190814 is a NS (Tews et al. 2021). In light of the constraints set by GW 170817, the determination of the stiffness can augment the GW channel to limit viable EOSs. Another aspect of utilizing the speed of sound to benefit astrophysics can be found in, e.g. Tews et al. (2018), where the authors build a family of nuclear interactions in terms of the behaviour of $v_{\rm s}$; thus, the inferred $v_{\rm s}$ from equation (23) limits the EOS model.

## 4 *G*-MODE CANDIDATE SYSTEMS

To better utilize the universal relations involving *g* modes developed in this article, we propose some candidate systems where *g*-mode detection may be plausible.

### 4.1 Precursor flares

For the NS progenitor of a merger, it has been proposed that mode resonance(s) may trigger precursor flashes of the SGRB following the merger, notably via interface (Tsang et al. 2012; Tsang 2013) and *g* modes (Kuan et al. 2021b) for slow-rotating NSs, and *f* and/or *r* modes for fast-spinning NSs (Suvorov & Kokkotas 2020). The uncertainties in both the spin rate of NS progenitors and the jet formation time-scale of the main episode allow for candidates of several kinds of mode, where the former quantity shifts the mode frequency relative to the orbital frequency inferred from the occurrence of precursors, and the latter time-scale blurs the amount of time prior to the merger.[3]

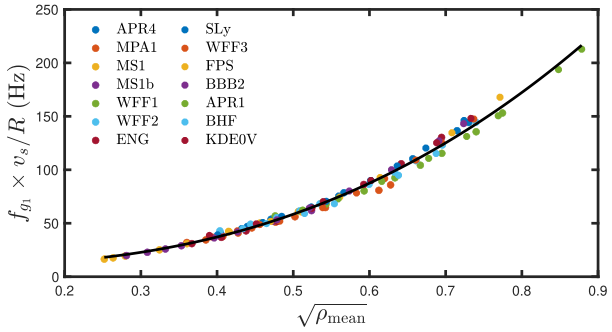


**Figure 9.** Rescaled $g_1$-mode frequency as a function of $\rho_{\rm mean}$ for the EOS considered here, with $v_{\rm s}$ being the central sound speed.

Seeing that NSs in coalescing binaries are expected to be mature and thus slowly rotating, we examine in a separate work (Kuan, Suvorov & Kokkotas in preparation) how two precursor flares (associated, for example, with GRB 090510; Troja, Rosswog & Gehrels 2010) can be accommodated by the lowest two orders of either *g* modes or interface modes. Nevertheless, the indicated spin rate of the host NS is $\lesssim$50 Hz for the former modes (see also below), while $\ll$10Hz is suggested by the latter modes. Even so, however, we emphasize here that we restrict ourselves to the *g*-mode resonance scenario (Kuan et al. 2021b), but other (e.g. *i* mode) possibilities exist (Tsang et al. 2012; Tsang 2013). The timing of precursors thus allows one to infer the (inertial-frame) frequency of the relevant mode, given by

$$\omega \simeq \omega_0 - 0.89m\Omega_{\rm s} \quad (25)$$

when the stellar magnetic field strength is small ($B \lesssim 10^{14}$ G), where $\omega_0$ is the free mode frequency (i.e. the frequency not accounting for tidal modulations to stellar structure), $\Omega_{\rm s}$ is the spin rate of the star, and $m$ is the winding number of the mode [cf. equation (70) in Kuan et al. (2021a)]. The numerical factor 0.89 arises by considering leading-order corrections in the slow-rotation approximation, though is also, in principle, sensitive to the compactness of the star (see fig. 10 in Kuan et al. 2021a).

For the specific case of SGRB 090510, the two precursors are detected when $\Omega_{\rm orb} \approx 160$ and 510 Hz, respectively. If they are attributed to $l = m = 2$ $g_1$ and $g_2$ modes of the star, we obtain the equalities

$$\omega_{\rm g_1} - 1.78\Omega_{\rm s} = 510\ {\rm Hz}, \quad (26a)$$

and

$$\omega_{\rm g_2} - 1.78\Omega_{\rm s} = 160\ {\rm Hz}, \quad (26b)$$

associating with the frequencies of the $g_1$ and $g_2$ modes of the primary. The notation $\omega = 2\pi f$ gives the angular frequency for linear frequency *f*. Exploiting the fact that the ratio between the frequencies of $g_1$ and $g_2$ modes is roughly a constant, viz. $\omega_{\rm g_2}/\omega_{\rm g_1} \simeq 0.68$ (equation 7), regardless the EOS and $\delta$, we deduce that $\omega_{\rm g_1} = 174 \times 2\pi$ Hz, $\omega_{\rm g_2} = 118 \times 2\pi$ Hz, and $\Omega_{\rm s} = 52.2 \times 2\pi$ Hz. The $g_1$-mode frequency can set a lower bound for $\delta$ since $\omega_1$ is smaller for

[3]Precursors can only be timed relative to the main burst by definition, which occurs only sometime after the merger since jet formation is not instantaneous, but has a development time-scale that depends on its formation mechanism (see section II. A of Suvorov & Kokkotas 2020, for a discussion).

decreasing $\delta$. In addition, although the ratio $\omega_{g_2}/\omega_{g_1}$ varies only slightly with respect to EOS and $\delta$, the difference $\omega_{g_1} - \omega_{g_2}$ requires $\delta$ to fall in certain range resulted from its dependence on $\delta$, as well as EOS. For instance, the difference of $\omega_{g_1} - \omega_{g_2} = 55.7 \times 2\pi$ Hz here restrains the stratification to be $0.008 \lesssim \delta \lesssim 0.2$ for EOS APR4, and $0.006 \lesssim \delta \lesssim 0.44$ for EOS ENG.

We should emphasize that aforementioned requirements for $\omega_{g_1}$, $\omega_{g_2}$, and $\delta$ are the necessary conditions for these two $g$ modes to be responsible for precursors; the sufficient condition is that the mode amplitude can be resonantly excited beyond certain threshold value (Kuan et al. 2021a,b). It turns out that the necessary and sufficient requirements are stringent for stellar parameters, and the viable region on the parameter space is expected to be narrow (see Kuan et al. 2021b, for a thorough discussion). None the less, we note that the EOSs of Group I are favoured in igniting precursors with moderately massive or light stars. Although the $g$-mode resonance in the quite massive ($\gtrsim 2$ M$_\odot$) or light ($\sim 1$ M$_\odot$) stars for the EOS of Group II is possible to fuel these early flares, it is unlikely that stars with EOS of Group III can host such pre-emissions.

In addition, the inferred $g_1$ mode is close to 200 Hz, which is marginally high in terms of its typical value $\sim$100 Hz. The tidal heating resulted from $g$ and $f$ modes investigated in Section 2.2 may pose a tension between the realizability of such frequency. None the less, it is possible for a spinning NS to have low-amplitude $r$-mode excitations, which may not slow down the star but still heat up the material to make the NS hot enough to admit such $g$ modes.

### 4.2 Quasi-periodic oscillations

Apart from the possibility of precursor flashes observed prior to merger events, there have not yet been direct $g$-mode observations in NSs, either of the nascent or mature variety. It has, however, been speculated by Strohmayer & Mahmoodifar (2014) that $g$ modes may be responsible for the QPOs observed in the X-ray light curves of AMXPs. While it is unclear which particular modes may be responsible in these cases (and indeed it is usually thought that *disc* $g$ modes may be responsible rather than *stellar* $g$ modes), it is necessary that their (inertial-frame) frequency matches that was observed, which is theoretically possible for the class of $g$ modes considered here.

We take XTE J1751−305 and XTE J1807−294 as examples since their QPO frequencies lie in the range of interest (i.e. $\lesssim$400 Hz). Although there are other possibilities, $r$ and $g$ modes are candidates for matching to these frequencies (Andersson, Jones & Ho 2014; Lee 2014; Strohmayer & Mahmoodifar 2014). The excitation of the former modes would generally be expected to sap angular momentum from the star also, especially if they are driven Chandrasekhar-Friedman-Schutz (CFS) unstable. However, at least for the specific outburst observed in XTE J1751−305, it is likely that if $r$ modes were responsible, the spin-up behaviour of the star following the first X-ray pulse in 2002 (the small variation in the flux is only observed in this stage) would have been lower (Andersson et al. 2014), which brings $g$ modes to our attention. Nevertheless, we emphasize that the trigger mechanism for QPOs is not well established, and we consider $g$ modes in this context to demonstrate how one may phenomenologically pin the pulsar in the $g_1$-space given an observation. The above-described scenario is represented by point (D) in Fig. 3.

According to equation (11), the mass, the radius, and the temperature of stars must be known in order to mark them on the $g$-space. Although we can deduce the mean density of two AMXPs, viz. the range of 0.919–1.214 for[4] XTE J1751−305 (Andersson et al. 2014), and the range of 0.499–1.425 for XTE J1807−294 (Leahy, Morsink & Chou 2011), the lack of the knowledge of their temperature prevents us from locating them on *g-space*. To better utilize the tool of $g$-space, future measurement of the temperature is crucial.

## 5 DISCUSSION

In this article, we investigate the dependence of $g$-mode frequencies on both microscopic (e.g. local changes in the adiabatic index) and macroscopic (e.g. stellar compactness) physics, revealing three families of EOS that still somehow support a number of universal relations. In particular, we found that $g$-mode frequencies correlate to the temperature-modified mean density to the power of a parameter $\varsigma$ (equation 11), where the range of $\varsigma$ divides EOS considered here (Table 1). This empirical fitting formulae define the *g-space*, where a given point corresponds to a unique EOS, which is split into three bands depending on $\varsigma$. Given some observations, from, e.g. precursors and QPOs, points can be pinned down in the *g-space* to scrutinize the EOS candidate (Fig. 3). Although joint constraints have been studied via Bayesian analysis in, e.g. Miller et al. (2019) and Raaijmakers et al. (2020, 2021), our approach here is not interlaced with uncertainties in the prior of the parametrization of the EOS. In addition, the applicability of equation (11) to $g_1$ to $g_3$ modes implies that the ratios between any two of them are roughly constant. Furthermore, if we are able to measure both $g_1$ and $g_2$ modes in a NS, e.g. from two precursors in an SGRB [the double events in GRB090510 may serve as an example (Kuan et al. 2021b)], we can measure the spin of the star within some tolerance by solving equations (26a) and (26b).

On top of the trifurcation, universal dependences of $g$ modes can be found in terms of certain quantities (equations 19–21). These pieces of EOS insensitive information can aid in placing constraints on EOS without a priori knowledge of the EOS. We show the universal sheet among the $g_1$-mode frequency, the tidal deformability, the stratification, and the mass of NSs (Fig. 4). Although inferring $\delta$ in a certain system is non-trivial, some estimates will be possible if we can measure additionally $f_{g_2}$. For a particular value of $\delta$, a specific section of the universal sheet will be picked up; assuming a typical value $\delta = 0.005$, we reduce the sheet to equation (19). For this $\delta$, we also establish the relation between $f_{g_1}$, $M$, and $\Lambda$ (equation 20). Three prospective applications of the above universal relations can be summarized as follows:

(i) Assuming we can measure $\mathcal{M}$, $\eta$, $\tilde{\Lambda}$, and $f_{g_1}$: the mass $M$, the radius $R$, and the $f$-mode frequency $f_f$ can be inferred from equations (19)–(21). The particular case of a GW170817-like binary is discussed in Section 3.1.

(ii) Assuming we can measure the $f$ and $g_1$ modes: a region of feasible models can be drawn on the mass-to-radius diagram (Fig. 8); such measurements are expected to be plausible with near-future detectors.

(iii) Given $\Lambda$ and the $f$-mode frequency: the $g_1$-mode value $f_{g_1}$ can be extracted via equation (23). In addition, the strong correlation between $f_f$ and $\rho_{mean}$ gives an estimate of the latter quantity, which

[4]Note that this density is inferred from the calculations in Andersson et al. (2014), who operated under the assumption that an $r$ mode was responsible for the outburst event, and it is therefore, strictly speaking, inconsistent to use their values in a $g$-mode analysis here. We adopt these values, however, to offer a proof of principle.

delegates $f_{g_1}$ on a certain region in Fig. 2, thus picking a certain group of EOS for the system.

Besides the global quantities, equation (24) sheds light on the central sound speed if the radius and the $g_1$-mode frequency are available. Seeing that the central sound speed of the NSs near the EOS-related maximal mass reflects the 'stiffness' of EOS, this indicates another aspect to disfavour certain range of 'stiffness' other than the analysis having been done to GW 170817, which is based on the measurement of $\tilde{\Lambda}$ (Abbott et al. 2018).

In addition, universal relations may also be leveraged to pin down observations on $g$-space if we can manoeuvre out of the observables mass, radius, and temperature of NSs. As a naïve example, we consider the remnant of merger. The transcendental information associating the tidal deformability of the *progenitors* of mergers to the compactness of the long-lived *remnant* [cf. equation (4) and fig. 9 of Manoharan et al. (2021)] says that we can learn the compactness of the remnant $\mathcal{C}_{\rm rem}$ from the measurement of $\tilde{\Lambda}$. In addition, the $f$-mode frequency of the remnant, $f_{\rm f,rem}$, may be measured from its influence on SGRB photon counts following the merger since the jet opening angle may widen and shorten as the star oscillates (Chirenti et al. 2019). Envisaging we have $f_{\rm f,rem}$ and $\mathcal{C}_{\rm rem}$, the five stellar parameters $f_{\rm g_1,rem}$, $f_{\rm f,rem}$, $M_{\rm rem}$, $R_{\rm rem}$, and $\Lambda_{\rm rem}$ of the remnant can be calculated by mutually solving equations (19)–(21). This information suffices to pin the system down in $g$-space within some tolerance.

To make further use of $g$-mode asteroseismology via the universal relations, we point out two possible avenues for detecting $g$ modes via electromagnetic sector, viz. the pre-emissions of SGRBs (Section 4.1) and (more speculatively) the QPOs in the X-ray light curve of AMXPs (Section 4.2). If the temperature in these systems can be measured somehow with future observatories (e.g. phase-resolved hotspot tracking for the latter), including the merger remnants, the $g$-mode ansatz introduced in this work, as well as the universal relations provided here, can be readily applied to place constraints on the EOS by identifying observations on *g-space*, as demonstrated in Fig. 3.

## ACKNOWLEDGEMENTS

CK gratefully acknowledges financial support by DFG research grant number 413873357. HJK recognizes support from Sandwich grant (JYP) number 109-2927-I-007-503 by DAAD and MOST during early stages of this work. We are grateful for the useful comments/suggestions given by the anonymous referee, which improved the quality of this article.

## DATA AVAILABILITY

Observational data used in this paper are quoted from the cited works. Data generated from computations are reported in the body of the paper. Additional data will be made available upon reasonable request.

## REFERENCES

Abbott B. P. et al., 2017, Phys. Rev. Lett., 119, 161101
Abbott B. P. et al., 2018, Phys. Rev. Lett., 121, 161101
Abbott B. P. et al., 2019, Phys. Rev. X, 9, 011001
Agrawal B. K., Shlomo S., Au V. K., 2005, Phys. Rev. C, 72, 014310
Akmal A., Pandharipande V. R., Ravenhall D. G., 1998, Phys. Rev. C, 58, 1804
Alford M., Braby M., Paris M., Reddy S., 2005, ApJ, 629, 969
Andersson N., Kokkotas K. D., 1998, MNRAS, 299, 1059
Andersson N., Pnigouras P., 2019, MNRAS, 489, 4043
Andersson N., Comer G. L., Glampedakis K., 2005, Nucl. Phys. A, 763, 212
Andersson N., Jones D. I., Ho W. C. G., 2014, MNRAS, 442, 1786
Arras P., Weinberg N. N., 2019, MNRAS, 486, 1424
Baldo M., Bombaci I., Burgio G. F., 1997, A&A, 328, 274
Beloborodov A. M., Li X., 2016, ApJ, 833, 261
Benitez E., Weller J., Guedes V., Chirenti C., Miller M. C., 2021, Phys. Rev. D, 103, 023007
Bizouard M.-A., Maturana-Russel P., Torres-Forné A., Obergaulinger M., Cerdá-Durán P., Christensen N., Font J. A., Meyer R., 2021, Phys. Rev. D, 103, 063006
Camelio G., Dietrich T., Rosswog S., Haskell B., 2021, Phys. Rev. D, 103, 063014
Capano C. D. et al., 2020, Nat. Astron., 4, 625
Chan T. K., Sham Y.-H., Leung P. T., Lin L.-M., 2014, Phys. Rev. D, 90, 124023
Chirenti C., Miller M. C., Strohmayer T., Camp J., 2019, ApJ, 884, L16
Coppin P., de Vries K. D., van Eijndhoven N., 2020, Phys. Rev. D, 102, 103014
Cromartie H. T. et al., 2019, Nat. Astron., 4, 72
Cutler C., Flanagan É. E., 1994, Phys. Rev. D, 49, 2658
Damour T., Nagar A., Villain L., 2012, Phys. Rev. D, 85, 123007
De S., Finstad D., Lattimer J. M., Brown D. A., Berger E., Biwer C. M., 2018, Phys. Rev. Lett., 121, 091102
Dietrich T., Coughlin M. W., Pang P. T. H., Bulla M., Heinzel J., Issa L., Tews I., Antier S., 2020, Science, 370, 1450
Douchin F., Haensel P., 2001, A&A, 380, 151
Duez M. D., Liu Y. T., Shapiro S. L., Stephens B. C., 2004, Phys. Rev. D, 69, 104030
Engvik L., Hjorth-Jensen M., Osnes E., Bao G., Ostgaard E., 1994, Phys. Rev. Lett., 73, 2650
Finn L. S., 1987, MNRAS, 227, 265
Flanagan É. É., Hinderer T., 2008, Phys. Rev. D, 77, 021502
Friedman B., Pandharipande V. R., 1981, Nucl. Phys. A, 361, 502
Fujibayashi S., Kiuchi K., Nishimura N., Sekiguchi Y., Shibata M., 2018, ApJ, 860, 64
Glendenning N. K., 1985, ApJ, 293, 470
Greif S. K., Hebeler K., Lattimer J. M., Pethick C. J., Schwenk A., 2020, ApJ, 901, 155
Haensel P., Levenfish K. P., Yakovlev D. G., 2002, A&A, 394, 213
Hinderer T., Lackey B. D., Lang R. N., Read J. S., 2010, Phys. Rev. D, 81, 123016
Hinderer T. et al., 2016, Phys. Rev. Lett., 116, 181101
Ho W. C. G., Lai D., 1999, MNRAS, 308, 153
Hoyos J., Reisenegger A., Valdivia J. A., 2008, A&A, 487, 789
Hoyos J. H., Reisenegger A., Valdivia J. A., 2010, MNRAS, 408, 1730
Kanakis-Pegios A., Koliogiannis P. S., Moustakidis C. C., 2020, Phys. Rev. C, 102, 055801
Kastaun W., Ciolfi R., Endrizzi A., Giacomazzo B., 2017, Phys. Rev. D, 96, 043019
Kiuchi K., Cerdá-Durán P., Kyutoku K., Sekiguchi Y., Shibata M., 2015, Phys. Rev. D, 92, 124034
Kokkotas K., Królak A., Tsegas G., 1994, Class. Quantum Gravity, 11, 1901
Kolomeitsev E. E., Voskresensky D. N., 2015, Phys. Rev. C, 91, 025805
Kowalska-Leszczynska I., Regimbau T., Bulik T., Dominik M., Belczynski K., 2015, A&A, 574, A58
Królak A., Kokkotas K. D., Schäfer G., 1995, Phys. Rev. D, 52, 2089
Krüger C. J., Kokkotas K. D., 2020, Phys. Rev. Lett., 125, 111106
Krüger C. J., Ho W. C. G., Andersson N., 2015, Phys. Rev. D, 92, 063009
Kuan H.-J., Suvorov A. G., Kokkotas K. D., 2021a, MNRAS, 506, 2985
Kuan H.-J., Suvorov A. G., Kokkotas K. D., 2021b, MNRAS, 508, 1732
Lackey B. D., Nayyar M., Owen B. J., 2006, Phys. Rev. D, 73, 024021
Lai D., 1994, MNRAS, 270, 611
Lai D., Wu Y., 2006, Phys. Rev. D, 74, 024007
Landry P., Essick R., Chatziioannou K., 2020, Phys. Rev. D, 101, 123007
Lau H. K., Leung P. T., Lin L. M., 2010, ApJ, 714, 1234
Leahy D. A., Morsink S. M., Chou Y., 2011, ApJ, 742, 17
Lee U., 2014, MNRAS, 442, 3037
Lindblom L., 1992, ApJ, 398, 569

McDermott P. N., van Horn H. M., Scholl J. F., 1983, ApJ, 268, 837
McDermott P. N., Hansen C. J., van Horn H. M., Buland R., 1985, ApJ, 297, L37
McDermott P. N., van Horn H. M., Hansen C. J., 1988, ApJ, 325, 725
Manoharan P., Krüger C. J., Kokkotas K. D., 2021, Phys. Rev. D, 104, 023005
Miller M. C., Chirenti C., Lamb F. K., 2019, ApJ, 888, 12
Moustakidis C. C., Gaitanos T., Margaritis C., Lalazissis G. A., 2017, Phys. Rev. C, 95, 045801
Mueller H., Serot B. D., 1996, Nucl. Phys. A, 606, 508
Müther H., Prakash M., Ainsworth T. L., 1987, Phys. Lett. B, 199, 469
O'Boyle M. F., Markakis C., Stergioulas N., Read J. S., 2020, Phys. Rev. D, 102, 083027
Oechslin R., Janka H.-T., Marek A., 2007, A&A, 467, 395
Oppenheimer J. R., Volkoff G. M., 1939, Phys. Rev., 55, 374
Ott C. D., Burrows A., Dessart L., Livne E., 2006, Phys. Rev. Lett., 96, 201102
Pang P. T. H., Tews I., Coughlin M. W., Bulla M., Van Den Broeck C., Dietrich T., 2021, ApJ, 922, 14
Passamonti A., Andersson N., Pnigouras P., 2021, MNRAS, 504, 1273
Perego A., Bernuzzi S., Radice D., 2019, Eur. Phys. J. A, 55, 124
Peters P. C., Mathews J., 1963, Phys. Rev., 131, 435
Potekhin A. Y., Yakovlev D. G., Chabrier G., Gnedin O. Y., 2003, ApJ, 594, 404
Prakash M., Ainsworth T. L., Lattimer J. M., 1988, Phys. Rev. Lett., 61, 2518
Prakash M., Cooke J. R., Lattimer J. M., 1995, Phys. Rev. D, 52, 661
Pratten G., Schmidt P., Hinderer T., 2020, Nat. Commun., 11, 2553
Press W. H., Teukolsky S. A., 1977, ApJ, 213, 183
Raaijmakers G. et al., 2020, ApJ, 893, L21
Raaijmakers G. et al., 2021, ApJ, 918, L29
Raithel C. A., Özel F., Psaltis D., 2018, ApJ, 857, L23
Read J. S., Lackey B. D., Owen B. J., Friedman J. L., 2009, Phys. Rev. D, 79, 124032
Reisenegger A., Goldreich P., 1992, ApJ, 395, 240
Schmidt P., Hinderer T., 2019, Phys. Rev. D, 100, 021501
Sherf Y., 2021, Phys. Rev. D, 103, 104003
Sotani H., Kumar B., 2021, Phys. Rev. D, 104, 123002
Sotani H., Takiwaki T., Togashi H., 2021, Phys. Rev. D, 104, 123009
Steinhoff J., Hinderer T., Dietrich T., Foucart F., 2021, Phys. Rev. Res., 3, 033129
Strohmayer T., Mahmoodifar S., 2014, ApJ, 784, 72
Suvorov A. G., Kokkotas K. D., 2020, Phys. Rev. D, 101, 083002
Tews I., Carlson J., Gandolfi S., Reddy S., 2018, ApJ, 860, 149
Tews I., Pang P. T. H., Dietrich T., Coughlin M. W., Antier S., Bulla M., Heinzel J., Issa L., 2021, ApJ, 908, L1
Tolman R. C., 1939, Phys. Rev., 55, 364
Torres-Forné A., Cerdá-Durán P., Obergaulinger M., Müller B., Font J. A., 2019, Phys. Rev. Lett., 123, 051102
Troja E., Rosswog S., Gehrels N., 2010, ApJ, 723, 1711
Tsang D., 2013, ApJ, 777, 103
Tsang D., Read J. S., Hinderer T., Piro A. L., Bondarescu R., 2012, Phys. Rev. Lett., 108, 011102
Van Oeveren E. D., Friedman J. L., 2017, Phys. Rev. D, 95, 083014
Wang J.-S., Peng Z.-K., Zou J.-H., Zhang B.-B., Zhang B., 2020, ApJ, 902, L42
Weih L. R., Most E. R., Rezzolla L., 2019, ApJ, 881, 73
Wiringa R. B., Fiks V., Fabrocini A., 1988, Phys. Rev. C, 38, 1010
Woosley S. E., Sukhbold T., Janka H.-T., 2020, ApJ, 896, 56
Yagi K., Yunes N., 2013, Phys. Rev. D, 88, 023009
Zhang N., Wen D., Chen H., 2019, Phys. Rev. C, 99, 035803

## APPENDIX A: TIDALLY NEUTRAL *G* MODES

In binaries, QNMs will be driven by the exertion of tidal forces from the companion. The resulting motions generate excess of gravitational energy by absorbing and localizing the orbital energy into the star. The 'efficiency' of the energy-soaking process for a specific mode is appraised by the overlap between the associated motion $\xi_{lnm}$ and the gravitational potential $\Phi^T$ of the companion (Press & Teukolsky 1977; Kuan et al. 2021a), where $\{nlm\}$ are conventional quantum numbers for harmonic oscillators. Considering solely the quadrupolar component ($l = 2$) of the potential, $\Phi^T_{\rm qd}$, due to its predominant contribution to tidal effects (see e.g. the discussion in appendix A.2 of Damour, Nagar & Villain 2012), tidal coupling strength of QNMs to the (leading-order) external tidal field is given by Kuan et al. (2021a)

$$Q_{nl} = \frac{1}{MR^l}\int {\rm d}\mathcal{V}\alpha(p+\rho)\bar{\xi}^{\mu}_{nll}\nabla_{\mu}\left(\Phi^T_{\rm qd}\right), \tag{A1}$$

which is independent of the winding number $m$. Here, ${\rm d}\mathcal{V}$ is the spatial volume form and $\alpha$ is the redshift factor, while $p$ denotes the pressure profile of the star. Equation (A1) indicates that only $l = 2$ QNMs are relevant to the leading-order tidal phenomena due to the orthogonality between spherical harmonic functions $Y_{lm}$.

Although only the absolute value of the tidal coupling $Q_{nl}$ matters in the context of energy absorption, we find that the $n = 1, l = 2\,g$ mode (quadrupolar $g_1$ mode) may have positive and negative values of $Q_{12}$, implying that there are some $g_1$ modes with $Q_{12} = 0$ from continuity (Rolle's theorem). For instance, we plot the tidal coupling of $g_1$ modes for several masses with EOS MPA1 in the top panel of Fig. A1, where each curve shows the $g_1$ modes with different stratification. We see that $g_1$ modes in the star with 1.59 $M_\odot$ have nearly vanishing $Q_{12}$, and may thus be fitting called 'tidally neutral'. By contrast, we find that $Q_{12}$ is always positive for the EOS belonging to *Group III* (see e.g. EOS PCL2 in the bottom panel of Fig. A1) except for EOS H7 and GNH3, whose models with mass close to the maximum have $Q_{12} \simeq 0$.

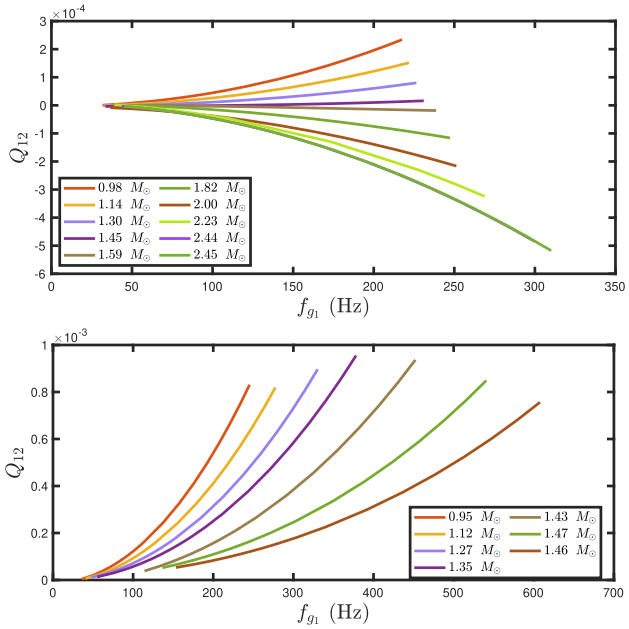


**Figure A1.** Tidal coupling strength as a function of $g_1$-mode frequency for several models of EOS MPA1 (top panel) and PCL2 (bottom panel). The mass of the star is held fixed for each curve shown here, which is drawn by increasing the stratification index $\delta$.

This paper has been typeset from a TEX/LATEX file prepared by the author.